Molecular Dynamics Simulation of Structure and Thermodynamic Properties of Poly(dimethylsilamethylene) and Hydrocarbon Solubility Therein: Toward the Development of Novel Membrane Materials for Hydrocarbon Separation

Vasilios E. Raptis,[†] Ioannis G. Economou,[*,†] Doros N. Theodorou,[†,§] John Petrou,[‡] and John H. Petropoulos[‡]

Molecular Modeling of Materials Laboratory, Institute of Physical Chemistry, National Research Center for Physical Sciences "Demokritos", GR-153 10 Aghia Paraskevi, Attikis, Greece, Study of Transport of Matter Phenomena Laboratory, Institute of Physical Chemistry, National Research Center for Physical Sciences "Demokritos", GR-153 10 Aghia Paraskevi, Attikis, Greece, and Department of Materials Science and Engineering, School of Chemical Engineering, National Technical University of Athens, 9 Heroon Polytechniou Street, GR-157 80 Athens, Greece

Received March 17, 2003; Revised Manuscript Received November 10, 2003

ABSTRACT: Molecular dynamics simulation is used to model the structure and thermodynamic properties of a novel rubbery polymer with promising membrane properties for hydrocarbon separation. A realistic united atom force field is developed based on extensive density functional theory quantum mechanics calculations for a model dimer and volumetric data at various temperatures and pressures. Both a constant bond length and a flexible bond length model are examined. Well-equilibrated structures of the polymer melt at various conditions are used to evaluate numerous thermodynamic properties, such as the isothermal compressibility, thermal expansion coefficient, and cohesive energy density, and structural properties, including intra- and intermolecular distribution functions and the static structure factor. The microscopic structure of the free volume of the polymer matrix and its evolution with time affects the diffusion of penetrant molecules considerably; they are calculated accurately using the Greenfield and Theodorou geometric analysis. The solubilities of various *n*-alkanes from methane to *n*-hexane at 300 and 400 K are calculated using the Widom test particle insertion technique. In all cases, simulation results are in good agreement with literature experimental data for the volumetric properties of the polymer melt and the solubility coefficients of *n*-alkanes in the polymer. In a forthcoming publication, the transport properties of these systems and the underlying molecular mechanisms will be examined.

1. Introduction

Permselective membranes are increasingly used today in a wide range of applications that include air separation, hydrogen separation, natural gas separation/fractionation, etc.[1] Membrane technology provides a number of advantages over other traditional technologies, such as low energy consumption, mild operating conditions, no environmental pollution, process continuity and flexibility, easy scalability, space savings, and modular plant design. The physicochemical properties that determine whether a given polymer is, in principle, suitable for a specific mixture separation are the sorption coefficient, S, and the diffusion coefficient, D, for each of the mixture components in the polymer. The permeability coefficient, $P = DS$, is further used for the calculation of permselectivity, $a_{A/B}$. For a specific binary mixture of components A and B, $a_{A/B} = P_A/P_B$. For industrial applications, P_i must be as high as possible whereas, at the same time, $a_{A/B}$ should be very different from unity to facilitate separation. In general, experimental data show that pairs of liquid and/or gas components with high permeability exhibit low permselectivity values, and vice versa.[2]

In most industrial applications utilizing polymeric membranes, glassy polymers are preferred.[3] In glassy polymers, permeselectivity is typically controlled by the diffusivity of the penetrants (diffusion controlling mechanism), so that these polymers normally operate by favoring passage of the lighter component(s) of the mixture.[4] On the other hand, permeability in rubbery polymers is mainly solubility driven, and so rubbery polymers are suitable for separation of mixtures where the heavy component(s) is (are) recovered.[4]

The diffusion coefficient and the solubility coefficient are macroscopic properties that depend strongly on the molecular structure of the polymer and penetrants and related microscopic mechanisms (i.e., intra- and intermolecular interactions, free-volume change etc.). Molecular simulation, using realistic force fields, is a powerful tool for the elucidation of molecular mechanisms and provides quantitative structure−macroscopic property relationships. For this reason, molecular simulation has become a design tool for novel polymeric materials with tailor-made end use properties.

This work is relevant to the design of a membrane process for the separation of natural gas heavy hydrocarbon components (C_{4+}) from the lighter components. A rubbery polymeric membrane is required. The most widely used rubbery membranes for industrial applications of this type are poly(dimethylsiloxane) and its derivatives.[5] However, the Si−O backbone bonds in these polymers are vulnerable to sulfuric compounds found in natural gas. In this work, a rubbery polymer containing Si−C bonds in the backbone, namely poly(dimethylsilamethylene) (PDMSM), is examined as a

* Corresponding author. E-mail: economou@mistras.chem.demokritos.gr.
[†] Molecular Modeling of Materials Laboratory, Institute of Physical Chemistry, National Research Center for Physical Sciences "Demokritos".
[‡] Study of Transport of Matter Phenomena Laboratory, Institute of Physical Chemistry, National Research Center for Physical Sciences "Demokritos".
[§] National Technical University of Athens.

10.1021/ma034332a CCC: $27.50
Published on Web 01/16/2004

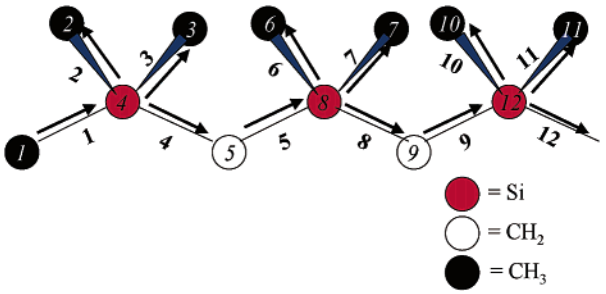

Figure 1. Schematic representation of PDMSM examined in this work.

potential membrane material.

Initially, a realistic united-atom (UA) force field is developed that describes accurately the *PVT* properties of the polymer melt over a wide temperature and pressure range. Polymer melts at various temperature and pressure values are examined based on extensive molecular dynamics (MD) simulations. A number of polymer melt configurations are analyzed using the Greenfield and Theodorou method[6] in order to determine the free-volume structure of the polymer and its change with time, which affects considerably the permeability of the hydrocarbon penetrants.

Subsequently, the infinite dilution solubility coefficient of various *n*-alkanes (methane through *n*-hexane) in PDMSM at 300 and 400 K is calculated using the Widom test particle insertion method. Finally, the enthalpy of sorption of *n*-alkanes in PDMSM is calculated. Simulation results are in excellent agreement with experimental data in all cases.

2. Force-Field Development

A schematic representation of the polymer examined in this work is given in Figure 1. In this scheme, hydrogen atoms in the methyl and methylene groups are not shown explicitly, in line with the UA force field developed here. UA force fields are used widely to model hydrocarbons,[7,8] polyolefins,[9] and other organic compounds with a high content in hydrogen atoms. This simplification does not affect the accuracy of the thermodynamic properties calculated through molecular simulation. Some deviation from all-atom force-field predictions may be possible for the transport properties of light penetrants (i.e., hydrogen, nitrogen, etc.) in the polymer.[10] However, this work focuses on the permeability of methane and heavier hydrocarbons in the polymer of interest, and so the UA force field is considered to be reliable for all properties calculated.

For chain molecules, the potential energy function is written in general as the sum of the contributions due to bond stretching, bond angle bending, dihedral angle torsion, and nonbonded intra- and intermolecular interactions, according to the general expression[11]

$$V_{\text{total}}(\mathbf{r}_1,...,\mathbf{r}_N) = V_{\text{stretching}} + V_{\text{bending}} + V_{\text{torsion}} + V_{\text{non-bonded}} = \sum_{\text{all bonds}} V(l_i) + \sum_{\text{all bond angles}} V(\theta_i) + \sum_{\text{all torsional angles}} V(\phi_i) + \sum_{\text{all pairs}} V(r_{ij}) \quad (1)$$

where l_i, θ_i, and φ_i denote bond length, bond angle, and torsional angle, respectively and r_{ij} is the distance between sites i and j. Bond stretching is much faster than bond angle bending and dihedral angle torsion and has relatively small effect on the physical properties examined here. Furthermore, by assuming bonds of constant length, a larger time step can be used to integrate the equations of motion in molecular dynamics. In the force field developed here, constant bonds were mainly used. However, to test the effect of bond stretching, representative calculations were performed with the same force field with the addition of a harmonic-type potential for bond stretching, of the form

$$V(l_i) = \frac{k_{l,i}}{2}(l_i - l_{i,o})^2 \quad (2)$$

A similar expression is used for bond angle bending, that is

$$V(\theta_i) = \frac{k_{\theta,i}}{2}(\theta_i - \theta_{i,o})^2 \quad (3)$$

In both eqs 2 and 3, subscript o denotes the value at the minimum of the respective potential.

For the torsional potential, almost always a cosine series expansion is used. The polymer under consideration possesses a single type of torsion angle, $CH_2-Si-CH_2-Si$. The following functional form is proposed, based on extensive quantum mechanical density functional theory (DFT) calculations, briefly discussed below:

$$V(\phi_i) = \frac{V_{\phi_i,o}}{2}(1 - \cos 3\phi_i) \quad (4)$$

Nonbonded intra- and intermolecular nonpolar interactions are calculated through a 6−12 Lennard-Jones potential:

$$V(r_{ij}) = 4\epsilon_{ij}\left[\left(\frac{\sigma_{ij}}{r_{ij}}\right)^{12} - \left(\frac{\sigma_{ij}}{r_{ij}}\right)^{6}\right] \quad (5)$$

where ϵ and σ are the energy and size Lennard-Jones parameters. Interactions between unlike segments ($i \neq j$) in the same or different molecules are calculated using the Lorentz−Berthelot combining rules:

$$\epsilon_{ij} = \sqrt{\epsilon_{ii}\epsilon_{jj}} \quad (6)$$

$$\sigma_{ij} = \frac{\sigma_{ii} + \sigma_{jj}}{2} \quad (7)$$

Bonded parameters in eqs 2−4 are typically calculated based on spectroscopic experimental data. For the polymer under consideration, no experimental data on structure were available, and so extensive quantum mechanics calculations were performed on a small model molecule resembling the corresponding dimer of PDMSM, that is di(trimethylsilyl)methane, $(CH_3)_3SiCH_2-Si(CH_2)_3$. Details of this work are given elsewhere,[12] and only a brief description is given here.

The main purpose of such calculations was to determine the minimum energy configuration, as well as the energy differences between that geometry and other representative configurations, characterized by specific bond and dihedral angle value combinations. Density functional theory (DFT)[13a−b] was employed. Specifically, the B3LYP[13c−d] functional with the 6-311G[13e−f] basis set was used. Unlike other levels of theory, e.g. Hartree−Fock, DFT accounts for electron correlation effects.

The B3LYP abbreviation corresponds to a hybrid functional given by the combination of a Becke three

parameter nonlocal functional (B3), describing the gradient-corrected exchange energy of electrons, and the nonlocal functional of Lee, Yang, and Parr (LYP), describing the gradient-corrected correlation energy of the electrons. The employed level of theory provides high accuracy at a moderate cost in CPU time, disk space and physical memory, in relation to perturbation and configuration interaction methods of comparable accuracy. 6-311G is a triple split valence basis set and assumes three sizes of contracted functions for each atomic orbital type. The selected basis set does not include diffuse or polarization functions, since the system is neutral and contains no lone-pair electrons. To ensure further that this basis set provides reliable results, more than 10 different points were examined thoroughly, including the minimum energy configuration, with the 6-311G** basis set, instead of the 6-311G one. Results and conclusions regarding geometry conformations and energy differences with the two basis sets were exactly the same. Therefore, it was securely determined that elimination of the polarization basis functions from the selected basis set is permissible; this resulted in an approximately 30% savings in CPU time (193 basis functions instead of 298 ones).

The structure with the global lowest energy is the one characterized as the equilibrium structure. Using those geometric parameters, a calculation of the frequencies of all vibrational modes was carried out and a determination of the zero-point energy (ZPE) was possible. This is the energy possessed by the vibrational modes of the system at the temperature of 0 K, as a result of Heisenberg's uncertainty principle. ZPE inclusion becomes essential for a proper determination of the energy difference between the minimum energy structure and any other molecular conformation of interest.

Di(trimethylsilyl)methane consists of 29 atoms (2 Si, 7 C, and 20 H). The starting geometric parameters were drawn from a previous similar molecular mechanics calculation.[13g] The equilibrium structure corresponds to the trans−trans configuration (with respect to the dihedrals of the backbone). Variation of these dihedral angles with a step size of 30° and minimization with respect to all other degrees of freedom than the torsion angles produced the conformational energy map. The symmetry of the conformational energy plot with respect to the two dihedrals of the dimer reflects the highly symmetric nature of the specific molecule. The functional form of eq 4 reflects this symmetry. $V_{\phi_i,o}$ was fitted to the energy barrier in the conformational energy map, and a value of 1.075 kcal/mol was obtained.

In addition, a series of calculations were carried out for structures near the equilibrium structure (torsion angles fixed in the trans state) with a slight variation (a step size of 1° was used) in (i) the silicon-central carbon−silicon angle, (ii) the methyl carbon−silicon−methyl carbon angle, and (iii) the methyl carbon−silicon−central carbon angle. The resulting energies (after minimization with respect to the remaining degrees of freedom) were used to parametrize the bonded potentials (bond length and bond angle, eqs 2 and 3). In the molecular simulations, both $Si-CH_3$ and $Si-CH_2$ bond lengths are set constant and equal to 1.91 Å, unless otherwise stated. Parameter values for the bond angles are given in Table 1.

Intramolecular Lennard-Jones interactions are divided into local and nonlocal interactions. Local Lennard-Jones interactions are those between sites that are three or four bonds apart (1−4 and 1−5 pairs, respectively). Nonlocal interactions are active between atoms that are farther apart. The Lennard-Jones parameters for the local interactions were also fitted to DFT results in order to reproduce the quantum mechanically calculated conformation energy map. Nonlocal parameters were set equal to the intermolecular Lennard-Jones parameters, fitted to polymer melt *PVT* properties as explained below. All Lennard-Jones parameter values are shown in Table 2.

Table 1. Parameters of the Force Field for the Bond Angles in PDMSM

bond angle (i)	$\theta_{i,o}$ (degrees)	$k_{\theta,i}$ (kcal/mol deg^2)
$Si-CH_2-Si$	123.06	0.034
$CH_2-Si-CH_2$	107.72	0.036
$CH_3-Si-CH_3$	109.23	0.026
$CH_3-Si-CH_2$	109.95	0.036

Table 2. Lennard-Jones Parameters for Local (1−4 and 1−5) Intramolecular and Nonlocal (1−6 and beyond) Intramolecular and Intermolecular Interactions

	local interactions		nonlocal interactions	
site	ϵ (kcal/mol)	σ (Å)	ϵ (kcal/mol)	σ (Å)
Si	0.791	2.370	0.585	3.385
CH_2	0.289	3.407	0.091	3.750
CH_3	0.289	3.407	0.210	4.106

3. Simulation Details

MD simulations were performed using a fifth-order Gear predictor−corrector algorithm for solving the equations of motion. Simulations with the constant bond length force field were based on the Edberg et al.[14] constrained dynamics scheme. The equations of motion were solved in Cartesian coordinates, utilizing holonomic constraints on the bond lengths.

As a result, the coordinates of each site are not independent. Constraint forces are evaluated by introducing appropriate Lagrange multipliers that prevent bonds from deformation. Introducing an index scheme to facilitate enumeration of the sites of the polymer (Figure 1), the dynamics of a chain molecule can be described by the following equations:

$$\ddot{\mathbf{r}}_1 = \frac{\mathbf{F}_1}{m_3} - \frac{\lambda_1}{m_3}\mathbf{R}_1 \tag{8}$$

$$\ddot{\mathbf{r}}_{4i-3} = \frac{\mathbf{F}_{4i-3}}{m_2} - \frac{\lambda_{4i-3}}{m_2}\mathbf{R}_{4i-3} + \frac{\lambda_{4(i-1)}}{m_2}\mathbf{R}_{4(i-1)} \quad i = 2,...,n \tag{9}$$

$$\ddot{\mathbf{r}}_{4i-2} = \frac{\mathbf{F}_{4i-2}}{m_3} - \frac{\lambda_{4i-2}}{m_3}\mathbf{R}_{4i-2} \quad i = 1,...,n \tag{10}$$

$$\ddot{\mathbf{r}}_{4i-1} = \frac{\mathbf{F}_{4i-1}}{m_3} - \frac{\lambda_{4i-1}}{m_3}\mathbf{R}_{4i-1} \quad i = 1,...,n \tag{11}$$

$$\ddot{\mathbf{r}}_{4i} = \frac{\mathbf{F}_{4i}}{m_1} + \frac{\lambda_{4i-3}}{m_1}\mathbf{R}_{4i-3} + \frac{\lambda_{4i-2}}{m_1}\mathbf{R}_{4i-2} + \frac{\lambda_{4i-1}}{m_1}\mathbf{R}_{4i-1} - \frac{\lambda_{4i}}{m_1}\mathbf{R}_{4i} \quad i = 1,...,n \tag{12}$$

$$\ddot{\mathbf{r}}_{4n+1} = \frac{\mathbf{F}_{4n+1}}{m_3} + \frac{\lambda_{4n}}{m_3}\mathbf{R}_{4n} \tag{13}$$

where n is the total number of monomer units (the

monomer unit is $CH_2Si(CH_3)_2$) per chain molecule, $\boldsymbol{F}_i$ is the force on site i due to the potential energy function $V(\boldsymbol{r}_1,...,\boldsymbol{r}_N)$, $\boldsymbol{R}_i$ is the corresponding bond vector ($\boldsymbol{R}_1 = \boldsymbol{r}_4 - \boldsymbol{r}_1$, $\boldsymbol{R}_{4i-3} = \boldsymbol{r}_{4i} - \boldsymbol{r}_{4i-3}$, $\boldsymbol{R}_{4i-2} = \boldsymbol{r}_{4i-2} - \boldsymbol{r}_{4i}$, $\boldsymbol{R}_{4i-1} = \boldsymbol{r}_{4i-1} - \boldsymbol{r}_{4i}$, $\boldsymbol{R}_{4i} = \boldsymbol{r}_{4i+1} - \boldsymbol{r}_{4i}$, $\boldsymbol{R}_{4n} = \boldsymbol{r}_{4n+1} - \boldsymbol{r}_{4n}$), λ_i is the Lagrange multiplier, and m_1, m_2, and m_3 are the masses of Si, CH_2, and CH_3 UA, respectively. Indices $4i$ and $4i - 3$ correspond to Si and CH_2 while all other indices correspond to CH_3.

The predictor−corrector scheme for the numerical solution of equations of motion in time introduces a small numerical error that propagates. The following penalty functions are minimized for each chain molecule when their values exceed a preset tolerance, to ensure proper chain structure:[14]

$$\Phi = \sum_{ij}(\mathbf{r}_{ij}^{\,2} - d_{ij}^{\,2})^2 \quad \text{(bond penalty function)} \tag{14}$$

$$\Psi = \sum_{ij}(\mathbf{r}_{ij}\cdot\dot{\mathbf{r}}_{ij})^2 \quad \text{(bond variation penalty function)} \tag{15}$$

The majority of MD calculations in this work were performed in the *NPT* ensemble. The extended statistical ensemble technique of Nosé and Klein was implemented.[15] In the extended ensemble under consideration, the following expanded Hamiltonian is conserved:

$$H = \sum_i \frac{\mathbf{p}_i^{\,2}}{2m_i s^2} + V_{\text{total}} + \frac{p_s^{\,2}}{2Q} + fkT\ln s + \frac{p_L^{\,2}}{18WL^4} + P_{\text{ext}}L^3 + \sum_n \lambda_n(\mathbf{R}_n^{\,2} - \mathbf{R}_0^2) \tag{16}$$

where

$$\mathbf{p}_i = m_i s^2 \dot{\mathbf{r}}_i, \quad p_s = Q\dot{s}, \quad p_L = 9WL^4\dot{L} \tag{17}$$

where $f = (4n + 1)N_{\text{ch}}$ is the number of degrees of freedom of the system, s is the degree of freedom corresponding to the heat bath used to control the temperature, L is the length of the box edge, W and Q are the inertia parameters associated with s and L, respectively, and P_{ext} is the externally set pressure. The equations of motion are derived in line with the procedure described in ref 16, p 47, taking into account the holonomic constraints imposed in order to fix the bond lengths.

The instantaneous pressure of the system, P_{int}, is calculated in the course of the simulation. It has been shown[17] that the molecular virial expression and the atomic virial expression for the instantaneous pressure provide practically the same results. Furthermore, the molecular virial is computationally faster as it requires only intermolecular interactions, and thus it is used in this work to evaluate the pressure. In this respect, the functional form proposed by Theodorou et al.[18] is used.

Finally, a Lennard-Jones truncated potential was used to ensure smooth transition to zero at long distances:

$$V_{ij}^{\text{LJ}} = \begin{cases} 4\epsilon_{ij}\left[\left(\dfrac{\sigma_{ij}}{r_{ij}}\right)^{12} - \left(\dfrac{\sigma_{ij}}{r_{ij}}\right)^{6}\right] & \text{if } 0 < r_{ij} < 1.45\sigma_{ij}; \\ \text{quintic spline}^{17} & \text{if } 1.45\sigma_{ij} < r_{ij} < 2.33\sigma_{ij}; \\ 0 & \text{if } 2.33\sigma_{ij} < r_{ij} \end{cases} \tag{18}$$

The appropriate tail corrections were computed to account for the truncation. The neighbor list technique (known also as the Verlet list[19]) was incorporated to reduce unnecessary computations.

The system used for the simulation of pure PDMSM melt consisted of three chains ($N_{\text{ch}} = 3$) with 80 monomeric units each ($n = 80$), that is 963 interacting sites in total. The molecular weight of the simulated polymer is 5775, a sufficiently high value for the accurate representation of physical properties of interest. In all cases, periodic boundary conditions were applied to the cubic simulation box, whose size was allowed to fluctuate during the run. In all cases, the initial structures were obtained using the Cerius[2] software package of Accelrys Inc. with the Dreiding force field.[20] A combination of the steepest descent and conjugate gradient methods was used for a fast and efficient minimization of the potential energy followed by 1 ns of MD simulation for equilibration. The criteria for equilibration used throughout this work were based on geometric characteristics of the chains (i.e., smooth torsion angle distribution) and on the stability of the running averages for the total energy and its constituents, and the density of the system. In all cases, such criteria were satisfied within the first ns of MD simulation. Production runs were at least 5 ns long. Throughout the MD runs, a constant time step of 0.5 fs was used.

In each production run, 5000 configurations were recorded at equal time intervals. These configurations were used for the calculation of various structure and thermodynamic properties of the polymer and for the evaluation of the chemical potential of light *n*-alkanes using the Widom test particle insertion method.[21]

According to Widom's method, the chemical potential is calculated from the ratio of the partition function of a system containing $N + 1$ molecules divided by the partition function of a system containing N molecules, where both systems are under the same conditions of temperature and volume or pressure. Here, the "ghost" molecule is an *n*-alkane molecule that is inserted randomly into the simulated system. The interaction energy of the "ghost" molecule with the remaining molecules (U_{ghost}) is evaluated and used for the calculation of the excess chemical potential (μ^{ex}) of the component:

$$\mu - \mu^{\text{ig}} \equiv \mu^{\text{ex}} = -\frac{1}{\beta}\ln\left[\frac{1}{\langle V\rangle_{NPT}}\langle V\langle\exp(-\beta U_{\text{ghost}}^{\text{intra}} - \beta U_{\text{ghost}}^{\text{inter}})\rangle_{\text{Widom}}\rangle_{NPT}\right] + \ln\langle\exp(-\beta U_{\text{ghost}}^{\text{intra}})\rangle_{\text{ideal gas}} \tag{19}$$

where $\beta = 1/kT$. The brackets in eq 19 denote ensemble averaging over all configurations and spatial averaging over all "ghost" molecule positions. Superscripts intra and inter refer to the intramolecular and intermolecular interactions, respectively. For methane, ethane and propane, the intramolecular interactions are zero.

To ensure good statistics, a large number of *n*-alkane molecule insertions were attempted per polymer configuration, from 10 000 insertions for methane up to 400 000 insertions for *n*-hexane. Furthermore, for *n*-butane, *n*-pentane, and *n*-hexane insertions a continuous configurational bias method was employed to facilitate insertion.[22] Such an approach has been shown

to be very effective for at least up to *n*-hexadecane molecule insertions.[22] The Henry's law constant of an *n*-alkane dissolved in the polymer can be easily evaluated from the expression:

$$H_{\text{alk}\rightarrow\text{pol}} = \lim_{x_{\text{alk}}\rightarrow 0}\left(\frac{\rho_{\text{pol}}RT}{\text{MW}_{\text{pol}}}\exp(\beta\mu^{\text{ex}}_{\text{alk}})\right) \qquad (20)$$

ρ_{pol} being the mass density of the polymer. For polymer mixtures, it is more convenient to use a Henry's law constant based on weight fractions, H', rather than based on mole fractions (given in eq 20). It is

$$H'_{\text{alk}\rightarrow\text{pol}} = H_{\text{alk}\rightarrow\text{pol}}\frac{MW_{\text{pol}}}{MW_{\text{alk}}} \qquad (21)$$

where MW_{alk} and MW_{pol} are the molecular weight values for the *n*-alkane and the polymer, respectively. The excess chemical potential may be also used for the calculation of the solubility coefficient at infinite dilution:

$$S_{\text{o}} = \frac{22400\ \text{cm}^3(STP)/\text{mol}}{RT}\lim_{x_{\text{alk}}\rightarrow 0}\exp(-\beta\mu^{\text{ex}}_{\text{alk}}) \qquad (22)$$

where S_{o} is in cm^3(STP)/(cm^3 pol atm).

4. Results and Discussion

4.1. Thermodynamic Properties of PDMSM Melt and Its Corresponding Oligomers. Lennard-Jones parameters for nonlocal intramolecular and intermolecular interactions were adjusted to reproduce best the polymer melt density at different temperature and pressure values and the density of tetramethylsilane, $Si(CH_3)_4$, along the saturation line. Initially, the Si Lennard-Jones parameters were set equal to the parameters proposed by Sok et al. for PDMS transport properties.[23] Sok et al. used an electrostatic term to model accurately the partly ionic character of the Si−O bond. On the other hand, the Si−C bond is largely covalent; thus, the Lennard-Jones potential is sufficient to describe nonbonded dispersion interactions. As a result, PDMS parameters for Si are only a first approximation.

For the case of CH_2 and CH_3 groups, both the TraPPE[7] and the NERD[8] models were considered. These two models were developed to reproduce accurately the saturated liquid and vapor densities and the vapor pressure of the entire homologous series of *n*-alkanes, including polyethylene oligomers. MD calculations at 300, 350, and 400 K and 0.1 MPa on the order of 5 ns each were performed and compared to experimental data from different sources. In all cases, the simulated melt density was of the order of 15% above the experimental value.

As the majority of Lennard-Jones sites in the polymer of interest are CH_3 (50%) and CH_2 (25%) groups and only 25% are Si atoms, an attempt was made to modify these group parameter values in a consistent way. In both TraPPE and NERD models for hydrocarbons, σ for CH_3 is smaller than σ for CH_2, which is physically unrealistic. Despite this deficiency, both models are very accurate for *n*-alkanes. In the model developed here for PDMSM, the following constraint was imposed: $\sigma_{CH_3} > \sigma_{CH_2}$.

The next step was to simulate $Si(CH_3)_4$ at the normal boiling point (280 K). A system of 120 molecules was simulated in the *NPT* ensemble. Six different sets of Lennard-Jones parameter values were tested in which either one or both ϵ and σ for CH_3 were varied by ±5% and ±10% about the corresponding TraPPE values. Each simulation lasted for 1 ns with a time-step of 0.5 fs. It turned out that density calculation is by far more sensitive to σ variation compared to ϵ variation. The optimum set of the nonlocal intramolecular and intermolecular parameters is shown in Table 2. This set was used subsequently for the calculation of saturated liquid density of $Si(CH_3)_4$ at 340 and 400 K, as shown in Figure 2. In all cases, excellent agreement was obtained between experimental data[24] and MD simulations. Furthermore, an *NPT* MD simulation was performed to calculate the density of $Si_2(CH_3)_6$ at 20 °C and 0.1 MPa. The resulting value was 0.769 g/cm^3 compared to the experimental one of 0.752 g/cm^3.[25]

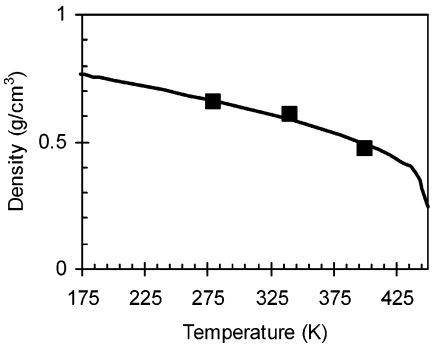

Figure 2. Saturated liquid density of $Si(CH_3)_4$. Experimental data (line[24]) and MD simulations (points) with the newly developed force field.

Table 3. Melt Density of PDMSM (in g/cm^3) from *NPT* MD Simulations at Various Temperatures and Pressures

P (MPa)	*T* = 300 K	*T* = 350 K	*T* = 400 K
0.1	0.927 ± 0.001	0.901 ± 0.0002	0.877 ± 0.0002
80	0.950 ± 0.002	0.936 ± 0.001	0.914 ± 0.001
160	0.968 ± 0.002	0.959 ± 0.001	0.941 ± 0.001

The new force field was subsequently used to calculate the PDMSM melt density at 300, 350, and 400 K. In each temperature, three different pressure values were examined that is 0.1, 80, and 160 MPa. The results are summarized in Table 3, and the statistical uncertainty reported is obtained from block averaging analysis (five blocks).

PDMSM melt densities in the temperature range 296−308 K and 0.1 MPa have been measured by several authors and there is agreement between different sources.[26−30] Furthermore, the MD calculation at 300 K is within less than 2% from these experimental data. Maier et al.[30] reported experimental *PVT* data for PDMSM over an extensive temperature (303−513 K) and pressure (0−200 MPa) range. There is considerable deviation between the data of Maier et al. and the data from all other sources. Furthermore, simulation results also deviate from these data by approximately 5%. In Figure 3, all literature experimental data and MD results are shown for comparison. In view of this scatter in the experimental data, no further adjustment of the force field was performed.

The volume fluctuations recorded during the MD simulation can be used to calculate the isothermal compressibility of the polymer melt, $\kappa_{\text{T}} = -(1/V)(\partial V/\partial P)_{\text{T}}$, based on the expression:

$$\kappa_{\text{T}} = \beta\frac{\langle V^2\rangle - \langle V\rangle^2}{\langle V\rangle} \qquad (23)$$

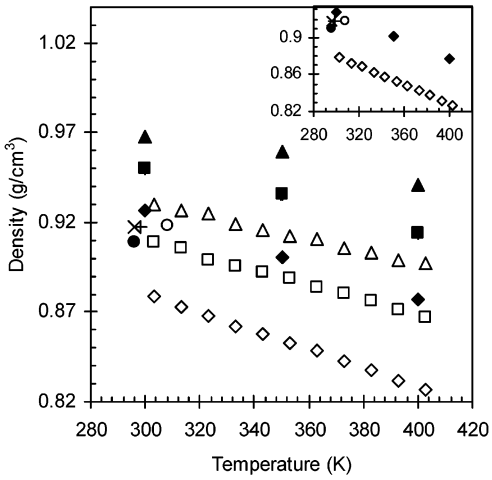

Figure 3. PDMSM melt density at different temperatures and pressures. Experimental data at 0.1 MPa (○ from ref 26; + from ref 27; × from ref 28; ● from ref 29; ◇ from ref 30), 80 MPa (□ from ref 30), and 160 MPa (△ from ref 30) and *NPT* MD simulations at 0.1 MPa (◆), 80 MPa (■), and 160 MPa (▲). In the inset, experimental data and MD simulations are shown for 0.1 MPa only.

Table 4. Isothermal Compressibility ($\kappa_T \times 10^4$ MPa^{-1}) of PDMSM from MD Simulations at Various Temperatures and Pressures

P (MPa)	*T* = 300 K	*T* = 350 K	*T* = 400 K
0.1	3.5 ± 1.0	4.9 ± 1.9	7.7 ± 3.4
80	3.6 ± 2.0	2.1 ± 0.7	4.5 ± 3.6
160	1.9 ± 1.2	2.3 ± 0.7	3.1 ± 1.3

In Table 4, MD simulation results are reported for various conditions. Experimental values of κ_T for PDMS are not available in the literature. For the majority of known polymers, κ_T is typically in the range $2-5 \times 10^{-4}$ MPa^{-1} .[31] From the Maier et al. *PVT* data,[30] a value of 4.2×10^{-4} MPa^{-1} is obtained at 300 K and 0.1 MPa, in good agreement with simulation results.

Furthermore, the thermal expansion coefficient, $\alpha_p = (1/V)(\partial V/\partial T)_P$, can be calculated numerically from the expression:

$$\alpha_p = \frac{\Delta\langle V\rangle}{\langle V\rangle \Delta T} \tag{24}$$

The MD simulation value at 300 K and 0.1 MPa is 0.58×10^{-3} K^{-1} whereas the experimental value is 0.6×10^{-3} K^{-1}.[26] Finally, the cohesive energy density, δ, from MD at 300 K and 0.1 MPa is equal to 8.5 ± 0.3 (cal/cm^3)$^{1/2}$, which compares very well with the experimental value of 8.02 (cal/cm^3)$^{1/2}$.[27]

All calculations reported so far were based on a force field with constant bond lengths. To quantify the effect of constant bonds, a harmonic potential was tested for bond stretching (eq 2) where $k_l = 128$ (kcal/mol)/Å^2 for all bonds. Each of three initially different configurations was subjected to two *NPT* MD simulations at 300 K and 0.1 MPa using the constant bond length and variable bond length potentials, respectively. In all cases, the simulation time was 1 ns for equilibration and 5 ns for production. The density predicted from the variable bond length potential was 0.5% higher than the density from the constant bond length potential (statistical uncertainty in density was less than 0.1%). The isothermal compressibility, κ_T, from the variable bond length potential was 24% higher than the value from the constant bond length potential (however the statistical uncertainty here is of the order of 10−25%) and the cohesive energy density, δ, from the two potentials was practically the same (within the statistical uncertainty of 2%). In conclusion, the introduction of flexible bonds has very small effects on the thermodynamic properties of the polymer melt.

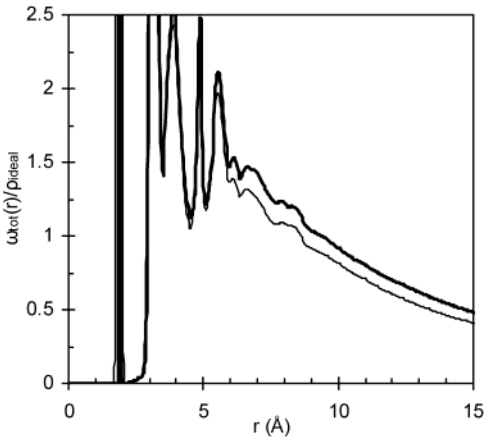

Figure 4. Total intramolecular pair distribution function $\omega_{tot.}(r)/\rho_{ideal}$ of PDMSM at 300 K and 0.1 MPa from *NPT* MD simulation (—, constant bond model; —, variable bond model).

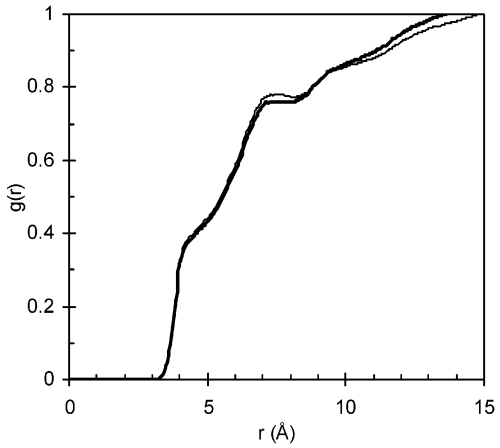

Figure 5. Total intermolecular pair distribution function $g_{tot.}(r)$, of PDMSM at 300 K and 0.1 MPa from *NPT* MD simulation (—, constant bond model; —, variable bond model).

4.2. Structural Properties of PDMSM. In the course of MD simulation, system configurations were stored every 1 ps and subsequently analyzed with respect to the structure and other properties of the polymer melt. The total intramolecular pair distribution function (all types of sites are taken into account), $\omega_{tot.}(r)/\rho_{ideal}$ ($\rho_{ideal} = n_{sites}/V$, where n_{sites} is the number of sites per chain and V is the volume of the simulation box) of PDMSM at 300 K and 0.1 MPa is shown in Figure 4. Calculations are shown for both constant bond and variable bond potentials. At small distances, intramolecular structures from the two models are practically identical. However, at longer distances, the variable bond potential results in slightly more contracted chains compared to the constant bond length one. This microscopic behavior is consistent with higher density values for the variable bond potential, as reported above.

In Figure 5, the total intermolecular pair distribution function $g_{tot.}(r)$ from the two models, at 300 K and 0.1 MPa is shown. The results are very similar, and only at long distances are some small deviations detected.

Intramolecular and intermolecular pair distribution functions were also calculated for the individual pairs

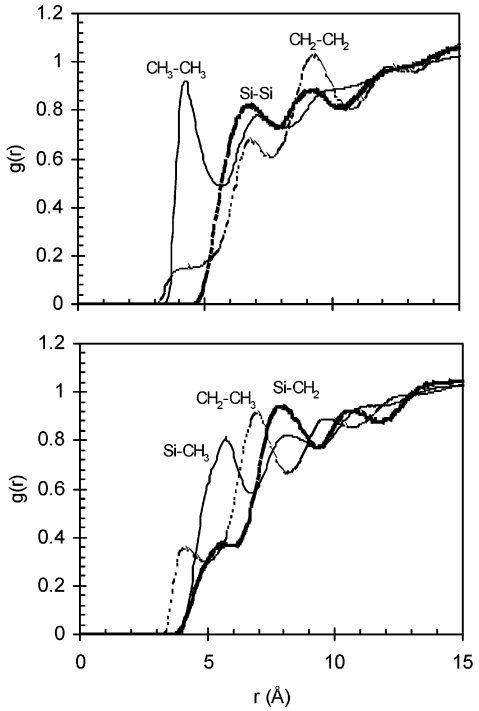

Figure 6. Intermolecular pair distribution functions for (top) Si−Si, CH_2-CH_2, and CH_3-CH_3 and (bottom) Si−CH_2, Si−CH_3, and CH_2-CH_3 of PDMSM at 300 K and 0.1 MPa using the constant bond potential from *NPT* MD simulation.

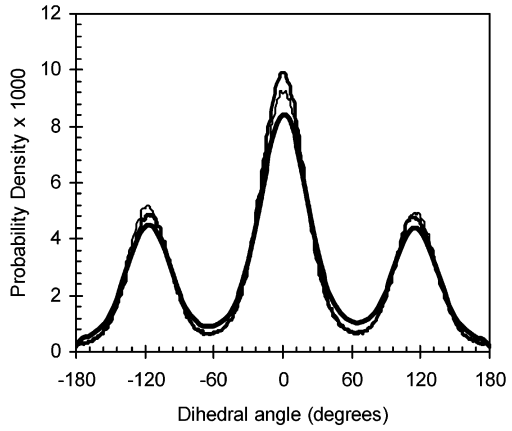

Figure 7. Dihedral angle distribution for PDMSM at 300 K and 0.1 MPa from the constant bond length (—) and variable bond length (−) models at 300 K and from the constant bond length (—) model at 400 K.

of the same (Si−Si, CH_2-CH_2, and CH_3-CH_3) or different (Si−CH_2, Si−CH_3, and CH_2-CH_3) types of sites. In Figure 6, results are shown for the intermolecular pair distribution function using the constant bond potential at 300 K and 0.1 MPa. Predictions from the variable bond potential are similar. At relatively short distances, $g_{CH_3-CH_3}(r)$ has a pronounced peak followed by a peak of lower height for $g_{Si-CH_3}(r)$. The remaining pairs of sites exhibit maximum values at relatively longer distances. No X-ray data are available in the literature to verify these predictions. In all cases, the behaviors are similar at 350 and 400 K, with the exception that the intensity of the peaks gradually decreases.

The dihedral angle distribution for PDMSM at 300 K and 0.1 MPa is shown in Figure 7. Although a 3-fold rotational symmetric torsional potential was adopted (eq 4), 1−4 nonbonded interactions result in a strong preference for the trans state (at 0°), compared to the gauche$^+$ and gauche$^-$ states. Furthermore, the bond flexibility tends to lower the occurrence of the trans state in favor of the other two states. At 400 K, the distribution around all three equilibrium states, as predicted from the constant bond potential, is broadened so that all three peaks are lowered, compared to 300 K.

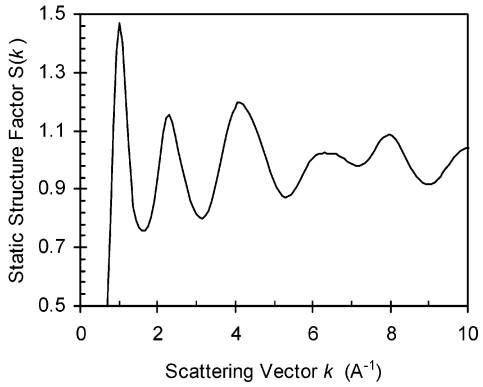

Figure 8. Static structure factor, $S(k)$, of PDMSM at 300 K and 0.1 MPa using the constant bond potential.

The structure of PDMSM melt was further examined through the static structure factor, obtained from a Fourier transform of the overall pair distribution function ($g_{tot.}(r) + \omega_{tot.}(r)/\rho_{ideal}$). Details of the calculation scheme used can be found in ref 17. The atomic structure factors used in the calculations were obtained from the literature.[32] In Figure 8, $S(k)$ at 300 K and 0.1 MPa is shown as a function of scattering vector, k. No experimental data are available for this polymer. The peak at low k values reflects intermolecular correlations, whereas at higher k values it reflects intramolecular correlations. Calculations from the flexible bond model are practically identical to the data from the constant bond length potential and are not shown here.

4.3. Free Volume Analysis of PDMSM. The free volume of the polymer accessible to penetrant molecules is a property that affects considerably both the solubility and diffusivity of these molecules. In this work, the melt structure of PDMSM was analyzed using the Greenfield and Theodorou technique.[6] The first step in the Greenfield−Theodorou approach is a geometric analysis of accessible volume within the polymer configuration. The goal of this geometric analysis is to determine (a) where within the polymer matrix, the center of a spherical penetrant-probe may reside, (b) how the shapes of these accessible regions are distributed and connected, and (c) how the accessible regions change with penetrant size.

The geometric analysis is performed for hard-sphere probes of various radii. For the purpose of this analysis, each polymer atom is assigned a hard-sphere radius (taken here as 0.99 of the Lennard-Jones radius of the atom). The first step in the analysis is a Delaunay tessellation of space within the polymer configuration into tetrahedra. Each Delaunay tetrahedron has its apices on four atoms that are nearest neighbors; it potentially defines an elementary interstitial space within the polymer (see Figure 1 in ref 6). The accessible volume inside each tetrahedron is then calculated for the considered probe radius; this is the volume, within the tetrahedron, wherein the center of the spherical probe may reside without overlapping with the polymer atoms. If the common triangular face between two tetrahedra is sufficiently open to allow passage of the

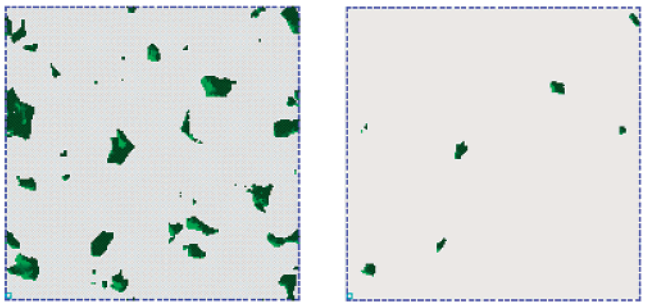

Figure 9. Accessible volume (shown in dark) for a typical PDMSM configuration at 300 K and 0.1 MPa for a penetrant molecule with hard-sphere radius of 1.4 Å (left) and for methane (right). The simulation box edge is 31.5 Å.

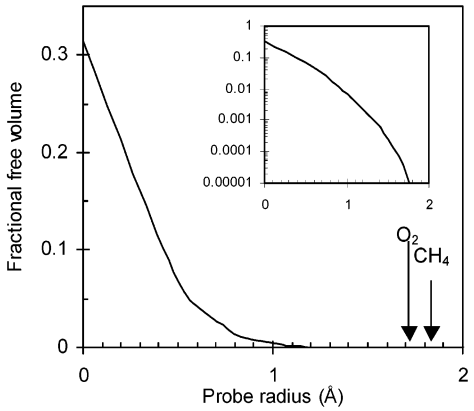

Figure 10. Fractional free volume for different probe radii for a typical PDMSM configuration at 300 K and 0.1 MPa using the Greenfield and Theodorou analysis.[6] In the inset, a logarithmic plot is shown for clarity.

spherical probe from the accessible region of one tetrahedron to that of the other, these tetrahedra are said to be connected. Using this criterion of connectedness, along with a clustering algorithm, the accessible space within the polymer is subdivided into clusters of accessible volume, each cluster consisting of several tetrahedra.

Clusters of accessible volume are determined for a range of hard-sphere probe radii, starting from a radius representative of the penetrant of interest and progressing to smaller and smaller radii, until percolation of accessible volume throughout the polymer configuration is observed. For large probe radii, accessible volume clusters tend to be few, small, and disjoint. As the probe radius is decreased, clusters grow in size and new clusters emerge. Clusters that were originally disconnected come together at "necks" of accessible volume and merge into single clusters.

In Figure 9, the clusters of accessible volume for a small penetrant (with a hard-sphere radius of 1.4 Å, left) and for methane (with a hard-sphere radius of 1.84 Å, right) are shown for a typical well-equilibrated PDMSM configuration. The accessible volume decreases dramatically as the penetrant molecule size increases. This is also evident from Figure 10, where the fractional free volume is shown as a function of the probe radius. Furthermore, in Figure 11, the cluster size distribution is shown for a penetrant of hard-sphere radius of 1.1 Å. The majority of clusters are of volume lower than 1.1 Å^3, and most of them are even below 0.5 Å^3. Only a few clusters have a volume larger than 2 Å^3.

For the diffusion process, the dynamic evolution of accessible volume of the polymer is very important. In

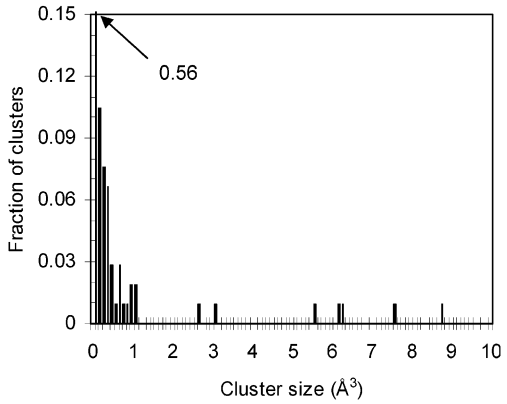

Figure 11. Cluster size distribution for a penetrant of hard-sphere radius equal to 1.1 Å.

glassy polymers, the characteristic times are very long so that the accessible volume undergoes very small changes even after several ns.[6] On the contrary, accessible volume changes fast in rubbery polymers. Figure 12 consists of a series of pictures, at different times, illustrating the clusters of accessible volume in a typical PDMSM configuration at 300 K and 0.1 MPa for (a) a methane penetrant and (b) a hard-sphere penetrant with 1.4 Å radius. The first picture in both cases was obtained after 4.91 ns of *NPT* MD. Each subsequent picture differs from the previous one by 10 ps. Interestingly, the topology of accessible volume changes considerably within the time frame examined, allowing relatively fast diffusion of the penetrant molecules. In both cases, relatively larger clusters prevail for a longer time compared to smaller clusters.

4.4. Solubility of *n*-Alkanes in PDMSM. The Widom test particle insertion method was used to calculate the excess chemical potential of *n*-alkanes, from methane to *n*-hexane, in PDMSM at 300 K and 0.1 MPa. In each of the 5000 PDMSM configurations taken from the MD simulation of the melt, a large number of *n*-alkane molecule insertions were attempted. As expected, for larger *n*-alkane molecules the rate of "successful insertions" decreases. A "successful insertion" is defined as the insertion where $r_{alk-pol} > 0.7\sigma_{alk-pol}$ for all inserted molecule and polymer segments, where $r_{alk-pol}$ is the distance between a segment of the inserted molecule and a polymer segment and $\sigma_{alk-pol}$ is the Lennard-Jones parameter for this pair of segments.

To maintain an approximately constant number of "successful insertions", the number of attempted insertions per configuration were as follows: 10 000 for methane, 20 000 for ethane, 50 000 for propane, 100 000 for *n*-butane, 200 000 for *n*-pentane, and 400 000 for *n*-hexane. In all cases, *n*-alkanes were modeled using the TraPPE force field, a very accurate model for the thermodynamic properties of such compounds.[7] In TraPPE, bond lengths are kept constant and equal to 1.54 Å for all C−C bonds.

Furthermore, to overcome problems associated with the slow relaxation of the polymer matrix that is not captured effectively by MD techniques and may affect μ^{ex} calculations significantly, a series of 6 ns long MD runs of PDMSM melt were performed at 300 K and 0.1 MPa with different initial configurations. Overall, 8 initially different structures were examined. Density, isothermal compressibility, and cohesive energy values from these runs were close to each other for all structures and to corresponding experimental values, ensur-

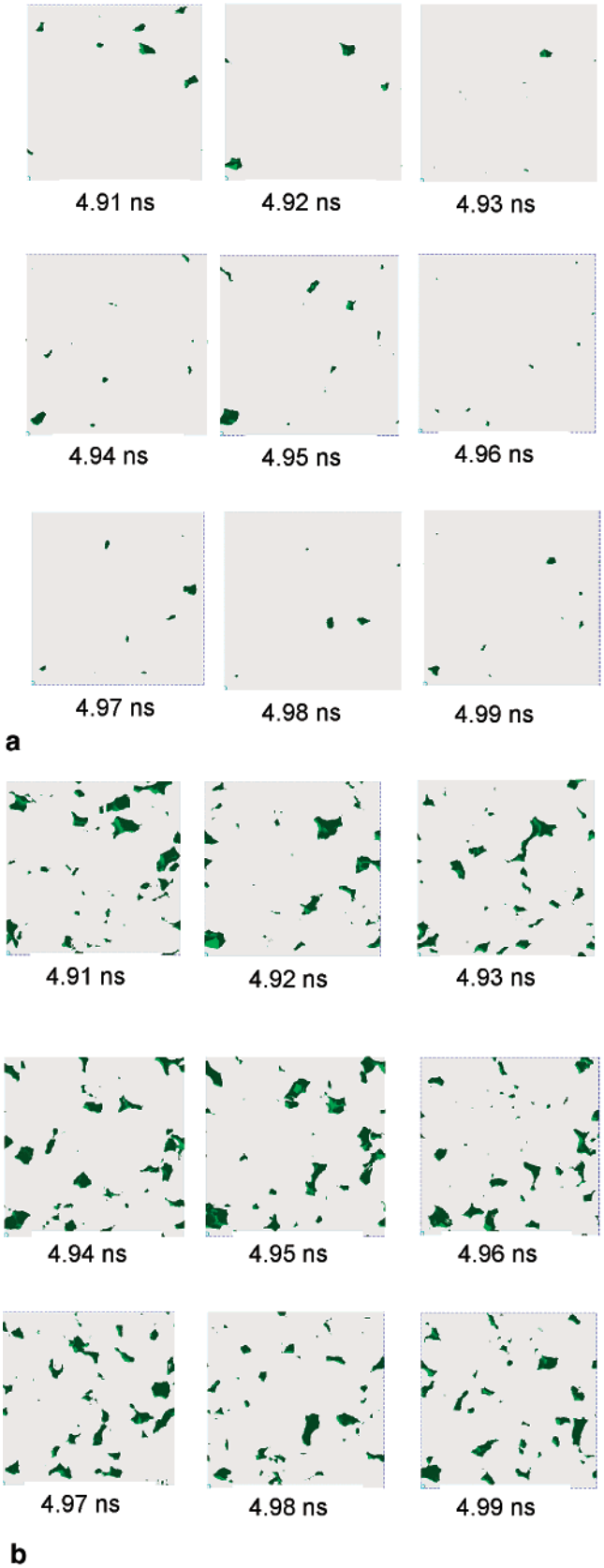

Figure 12. Evolution of accessible volume (shown in dark) for PDMSM at 300 K and 0.1 MPa for (a) a methane molecule, and (b) a spherical molecule of hard sphere radius of 1.4 Å. The time indicated for each configuration is the elapsed time from the beginning of the MD simulation. The simulation box edge is 31.5 Å.

ing that all structures are realistic representations of PDMSM. More specifically, $\rho_{pol} = 0.924 \pm 0.001$ g/cm^3,

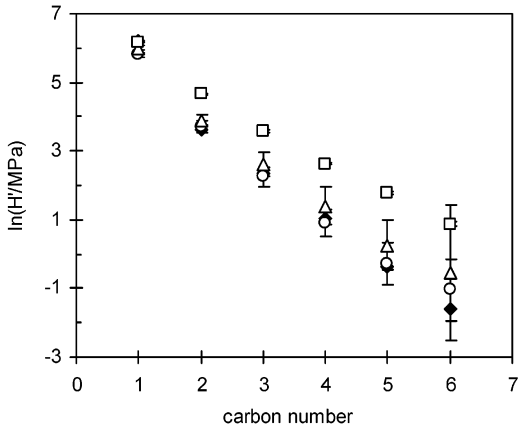

Figure 13. Weight fraction Henry's law constant of *n*-alkanes in PDMSM at 300 K and 0.1 MPa. Experimental data[28,33] (◆) and molecular simulation predictions from the constant bond length (○) and variable bond length (△) models are given. Molecular simulation predictions at 400 K and 0.1 MPa using the constant bond length model are also shown (□).

$\kappa_T = (3.6 \pm 0.4) \times 10^{-4}$ MPa, and $\delta = 8.46 \pm 0.03$ (cal/cm^3)$^{1/2}$. The stored configurations from each MD run were also used for Widom test particle insertions.

On the basis of the μ^{ex} values for *n*-alkanes in PDMSM, the Henry's law constant (eq 21) and the solubility coefficient at infinite dilution, S_o (eq 22), were calculated. In Figure 13 experimental data and MD results for the weight fraction based Henry's constant are presented whereas in Table 5 experimental data and MD simulation results are shown for S_o. The agreement is very good in all cases. The statistical uncertainty reported in the simulations is the standard deviation in the calculations over the eight different structures. For the larger of the *n*-alkanes examined (especially *n*-pentane and *n*-hexane), the statistical uncertainty remains high, despite the many different structures examined and the large number of particle insertions.

The excess chemical potential of *n*-alkanes was also calculated using the variable bond length model. In this case, calculations were based on three initially different structures for PDMSM. All other simulation parameters (duration, *n*-alkane insertions, etc.) were the same as above. The thermodynamic properties for the PDMSM melt from this model were $\rho_{pol} = 0.9289 \pm 0.0005$ g/cm^3, $\kappa_T = (4.3 \pm 1.1) \times 10^{-4}$ MPa, and $\delta = 8.5 \pm 0.1$ (cal/cm^3)$^{1/2}$. Solubility coefficient calculations for the *n*-alkanes are shown in Table 5; they correspond to the Henry's law constants presented in Figure 13. Interestingly, the variable bond calculations for S_o are consistently lower than the corresponding calculations from the constant bond model (with the exception of *n*-hexane). This can be attributed partly to the larger density of the variable bond model that results in lower free volume for successful penetrant insertions. For the larger *n*-alkanes, the difference is within the statistical uncertainty of the calculations, and thus additional work is needed to resolve this difference.

The excess chemical potential of *n*-alkanes in PDMSM was calculated also at 400 K and 0.1 MPa. Four initially different structures of pure PDMSM melt were simulated with the constant bond potential for a total of 6 ns: 1 ns for equilibration and 5 ns for production to generate the 5000 configurations in each case needed for the subsequent Widom insertions. The total number of attempted insertions of *n*-alkane molecules per configuration was the same as in 300 K. In Table 5, the

Table 5. Experimental Data and Molecular Simulation Results from the Constant Bond Length (const) Model at 300 K and 0.1 MPa and 400 K and 0.1 MPa and the Variable Bond Length (var) Model at 300 K and 0.1 MPa for the Infinite Dilution Solubility Coefficient, S_o, of *n*-Alkanes in PDMSM

	S_o (cm^3(STP)/cm^3 pol/atm)			
n-alkane	experiment 300 K	simulation (const) 300 K	simulation (var) 300 K	simulation (const) 400 K
methane	0.335[a]	0.39 ± 0.04	0.33 ± 0.03	0.19 ± 0.01
ethane	2.40[b]	1.8 ± 0.3	1.4 ± 0.2	0.48 ± 0.01
propane	5.81[a]	5.2 ± 1.7	3.7 ± 1.3	0.95 ± 0.02
n-butane	16.5[b]	16 ± 7	10 ± 5	1.87 ± 0.05
n-pentane	52.7[b]	46 ± 30	27 ± 17	3.5 ± 0.2
n-hexane	152.2[b]	93 ± 64	171 ± 98	7.2 ± 0.5

[a] From ref 28. [b] From ref 33 (for ethane, it is an estimation based on an empirical correlation).

Table 6. Experimental Data[33] and Molecular Simulation Results from the Constant Bond Length Model for the Enthalpy of Sorption (ΔH_s) of *n*-Alkanes in PDMSM

	$-\Delta H_s$ (kcal/mol)	
n-alkane	experiment	simulation
methane		1.7 ± 0.2
ethane		3.1 ± 0.4
propane	3.2 ± 0.4	4.1 ± 0.8
n-butane	4.8 ± 0.6	5.1 ± 1.0
n-pentane	5.8 ± 0.7	6.2 ± 1.6
n-hexane	6.8 ± 0.9	6.1 ± 1.7

infinite dilution solubility coefficient values are reported, and in Figure 13, the Henry's law constants are shown. A significant decrease in S_o is observed at 400 K compared to 300 K, which is more pronounced for the case of heavier *n*-alkanes. Similar behavior has been observed experimentally for the case of various *n*-alkanes and α-olefins in low-density polyethylene.[34] No experimental data are available in the literature for PDMSM at this elevated temperature.

Molecular simulation results were used subsequently to calculate the enthalpy of sorption (ΔH_s) of *n*-alkanes in PDMSM, based on the expression

$$\frac{\partial(\ln S_o)}{\partial(1/T)} = -\frac{\Delta H_s}{R} \tag{25}$$

Experimental data[33] and molecular simulation results using the constant bond model for ΔH_s are shown in Table 6. Model predictions are in excellent agreement with experimental measurements for propane through *n*-hexane. No experimental data were available for methane and ethane.

5. Conclusions

In this work, a new UA force field was developed for a rubbery polymer, namely poly(dimethylsilamethylene), based on DFT quantum mechanics calculations on a model dimer molecule and MD simulations for the corresponding monomer and the polymer melt at different temperatures and pressures. PDMSM is considered a promising novel membrane material for hydrocarbon separation.[33] As a result, accurate representation of its physical properties and free-volume structure is of great importance. The force field represents well the volumetric properties of the polymer in the temperature range 300−400 K and pressure range 0.1−160 MPa.

Equilibrated configurations of the polymer melt were analyzed with respect to the molecular structure of the polymer (intra- and intermolecular radial distribution functions, structure factor, torsion angle distribution). The Greenfield and Theodorou technique was applied to quantify the free-volume structure and the microcavities accessible to small penetrant molecules were characterized with respect to size, concentration, and change with time.

The solubility of *n*-alkanes from methane to *n*-hexane in PDMSM at 300 and 400 K was calculated based on the Widom test particle insertion method. Simulation results were in excellent agreement with experimental data at 300 K. In addition, the enthalpy of sorption of *n*-alkanes in PDMSM was calculated from the simulation results and shown to be in good agreement with available experimental data.

Molecular dynamic simulations for the evaluation of the transport properties of *n*-alkanes in PDMSM are underway. In this case, much longer MD simulations are needed, on the order of a few tens of nanoseconds. Furthermore, the molecular mechanisms that control the macroscopic transport properties are elucidated. This will be the subject of a forthcoming publication.

In conclusion, this work indicates that molecular simulation is a powerful tool for exploring the properties of novel complex materials for major industrial applications.

Acknowledgment. Financial support by the NATO Science for Peace Program (Project No. 972638 on "Novel Membranes") and the Greek General Secretariat of Research and Technology is gratefully acknowledged. V.E.R. is thankful to the CINECA Supercomputing Center in Bologna, Italy, for a visiting fellowship and generous allocation of supercomputing time. We are indebted to Niki Vergadou for assistance in free-volume calculations and in generating Figures 9−12.

References and Notes

(1) Baker, R. W. *Ind. Eng. Chem. Res.* **2002**, *41*, 1393.
(2) Robeson, L. M.; Burgoyne, W. F.; Langsam, M.; Savoca, A. C.; Tien, C. F. *Polymer* **1994**, *35*, 4970.
(3) Paul, D. R., Yampolskii, Yu. P., Eds. *Polymeric Gas Separation Membranes*; CRC Press: Boca Raton, FL, 1994.
(4) Petropoulos, J. H. Chapter 2 in ref 3.
(5) Schultz, J.; Peinemann, K.-V. *J. Membr. Sci.* **1996**, *110*, 37.
(6) Greenfield, M.; Theodorou, D. N. *Macromolecules* **1993**, *26*, 5461.
(7) Martin, M. G.; Siepmann, J. I. *J. Phys. Chem. B* **1998**, *102*, 2569.
(8) Nath, S. K.; Escobedo, F. A.; de Pablo, J. J. *J. Chem. Phys.* **1998**, *108*, 9905.
(9) Mavrantzas, V. G.; Boone, T. D.; Zervopoulou, E.; Theodorou, D. N. *Macromolecules* **1999**, *32*, 5072.
(10) Ungerer, P.; Beauvais, C.; Delhommelle, J.; Boutin, A.; Rousseau, B.; Fuchs, A. H. *J. Chem. Phys.* **2000**, *112*, 5499.
(11) Leach, A. R. *Molecular Modelling: Principles and Applications*, Addison-Wesley Longman Ltd.: Harlow, England, 1996.
(12) Melissas, V. S.; Raptis, V. E.; Hatzopoulou, E. G.; Economou, I. G.; Theodorou, D. N. Manuscript in preparation.

(13) (a) Hohenberg, P.; Kohn, W. *Phys. Rev.* **1964**, *136*, B864. (b) Kohn, W.; Sham, L. J. *Phys. Rev.* **1965**, *140*, A1133. (c) Becke, A. D. *J. Chem. Phys.* **1993**, *98*, 5648. (d) Lee, C.; Yang, W.; Parr, R. G. *Phys. Rev. B* **1988**, *37*, 785. (e) McLean, A. D.; Chandler, G. S. *J. Chem. Phys.* **1980**, *72*, 5639. (f) Krishnan, R.; Binkley, J. S.; Seeger, R.; Pople, J. A. *J. Chem. Phys.* **1980**, *72*, 650. (g) Hyperchem, version 5.1.
(14) Edberg, R.; Evans, D. J.; Morriss, G. P. *J. Chem. Phys.* **1986**, *84*, 6933.
(15) Nosé, S.; Klein, M. L. *Mol. Phys.* **1983**, *50*, 1055.
(16) Goldstein, H. *Classical Mechanics*, 2nd ed., Narosa Publishing House: New Delhi, 1993.
(17) Antoniadis, S. J.; Samara, C. T.; Theodorou, D. N. *Macromolecules* **1998**, *31*, 7944.
(18) Theodorou, D. N.; Boone, T. D.; Dodd, L. R.; Mansfield, K. F. *Makromol. Chem., Theory Simul.* **1993**, *2*, 191.
(19) Allen, M. P.; Tildesley, D. J. *Computer Simulation of Liquids*, Oxford Science Publications: Oxford, England, 1987.
(20) Mayo, S. L.; Olafson, B. D.; Goddard, W. A., III. *J. Phys. Chem.* **1990**, *94*, 8897.
(21) Widom, B. *J. Chem. Phys.* **1963**, *39*, 2808.
(22) Spyriouni, T.; Economou, I. G.; Theodorou, D. N. *Macromolecules* **1997**, *30*, 4744.
(23) Sok, R. M.; Berendsen, H. J. C.; van Gunsteren, W. F. *J. Chem. Phys.* **1992**, *29*, 3615.
(24) DIPPR *Data Compilation of Pure Compound Properties*; AIChE: New York, 1997.
(25) Holroyd, R.; Itoh, K.; Nishikawa, M. *Nucl. Inst. Methods Phys. Res. A* **1997**, *390*, 233.
(26) Ko, J. H.; Mark, J. E. *Macromolecules* **1975**, *8*, 869.
(27) Bhide, B. D.; Stern S. A. *J. Appl. Polym. Sci.* **1991**, *42*, 2397.
(28) Shah, V. M.; Hardy, B. J.; Stern, S. A. *J. Polym. Sci., Polym. Phys.* **1993**, *31*, 313.
(29) Finkelshtein E. S. Unpublished results, 1999.
(30) Maier, R. D.; Kopf, M.; Mäder, D.; Koopmann, F.; Frey, H.; Kressler, J. *Acta Polym.* **1998**, *49*, 356.
(31) Van Krevelen, D. W. *Properties of Polymers*, 3rd ed.; Elsevier: Amsterdam, 1990.
(32) Atomic structure factors for Si were obtained from: *International Tables for X-ray Crystallography*; Iber, J. A., Hamilton, W. C., Eds.; Kluwer Academic Publishers: Amsterdam, 1989; Vol. IV (Revised and Supplementary Tables), Table 2.2A. Those for CH_3 and CH_2 were obtained from: Narten, A. H. *J. Chem. Phys.* **1979**, *70*, 299.
(33) Soloviev, S. A.; Yampolskii, Yu. P.; Economou, I. G.; Ushakov, N. V.; Finkelshtein, E. Sh. *Polym. Sci. Ser. A* **2002**, *44*, 293.
(34) Maloney, D. P.; Prausnitz, J. M. *AIChE J.* **1976**, *22*, 74.

MA034332A